

Inverse cascade anomalies in fourth-order Leith models

Simon Thalabard,^{1,2, a)} Sergey Medvedev,^{3,4, b)} Vladimir Grebenev,^{3, c)} and Sergey Nazarenko^{2, d)}

¹⁾*Instituto Nacional de Matemática Pura e Aplicada – IMPA, 22460-320 Rio de Janeiro, Brazil*

²⁾*Institut de Physique de Nice, Université Côte D’Azur et CNRS, Nice 06108, France*

³⁾*Federal Research Center for Information and Computational Technologies, Novosibirsk 630090, Russia*

⁴⁾*Novosibirsk State University, Novosibirsk 630090, Russia*

We analyze a family of fourth-order non-linear diffusion models corresponding to local approximations of 4-wave kinetic equations of weak wave turbulence. We focus on a class of parameters for which a dual cascade behavior is expected with an infrared finite-time singularity associated to inverse transfer of waveaction. This case is relevant for wave turbulence arising in the Nonlinear Schrödinger model and for the gravitational waves in the Einstein’s vacuum field model. We show that inverse transfer is not described by a scaling of the constant-flux solution but has an anomalous scaling. We compute the anomalous exponents and analyze their origin using the theory of dynamical systems.

^{a)}Electronic mail: simon.thalabard@inphyni.cnrs.fr

^{b)}Electronic mail: serbormed@gmail.com

^{c)}Electronic mail: vngrebenev@gmail.com

^{d)}Electronic mail: Sergey.NAZARENKO@unice.fr

I. FROM KINETIC EQUATIONS TO NON-LINEAR DIFFUSIONS

Single cascade and second-order diffusions. The differential approximation model (DAM) introduced by Cecil Leith in the context of two-point spectral closures for fully-developed homogeneous isotropic turbulence¹ provides a class of tractable models with two desirable features: (i) compatibility with thermodynamics, that allows both for the Lee equilibrium states² and the Kolmogorov cascade solutions to emerge and (ii) connection to kinetic equations, *e.g.* spectral closures featuring integro-differential approximations under a Markovian approximation are known to reduce to non-linear diffusions when interactions are restricted onto well-chosen subclasses of local triads^{1,3,4}. Leith's approximation can be thought of as a type of non-linear Fourier law, where the energy flux is written as a non-linear function of the energy spectrum and of its spectral derivative. As such, the approximation is of *second-order* and it provides a flexible framework to address fluid systems whose physics can be reduced to single conservation laws. While Leith's original model is too crude to produce quantitatively precise results for strong turbulence⁵, it describes robust qualitative features of turbulence beyond the properties that are hardwired into it, *e.g.* the Kolmogorov and the thermodynamic steady states. In particular, the model has a stationary solution in the form of a mixed Kolmogorov-thermodynamic state –the so-called “warm cascade”⁶. Further, its generalization has proven fruitful to get qualitative insights in various turbulent settings. For atmospheric turbulence, it was used to substantiate the origin of the Nastrom-Gage spectrum of atmospheric turbulence in terms of a dual cascade state, involving energy and enstrophy flowing through a common inertial range of scales^{7,8}. Another salient generalization of Leith model coupling superfluid and normal-fluid components via a mutual friction has allowed to unveil interesting new scaling states relevant for superfluid turbulence^{9,10}. Besides, Leith type models also found relevance in the context of passive transport and wave turbulence¹¹, where they have proven useful to address non-stationary dynamics.

Among salient features, second-order models with finite capacity are now known to feature self-similar finite-time blow-up with anomalous scaling; this observation holds true for a wide class of systems¹¹ including the original Leith model⁶, but also systems featuring inverse cascade behavior¹². What makes the diffusion approximation particularly valuable is the fact that unlike other classes of closures^{13,14}, the diffusion structure allows for the mathematical analysis of the anomalous transients. In particular, it was recently found that those can be analyzed in terms of self-similar solutions of the second-kind¹⁵, where a self-similar profile develops in finite time over

an infinite range of scales, featuring a sharp front on one side and an anomalous algebraic decay on the other side of the spectral range.

Dual cascades and fourth-order diffusions. Generalized DAM describing single-conservation laws can be heuristically derived from dimensional analysis¹⁶ to gain insights on the behavior of the relevant kinetic equations. An obvious shortcoming of such second-order DAM is their inability to address dual cascade scenario—a building block of wave-turbulence. To model systems with two conservation laws within a diffusion approximation, one has to rely on another class of DAM, later referred to as *fourth-order models*. Beyond the case of two-dimensional (2D) turbulence¹⁷, fourth-order DAM find applications in wave systems relevant for classical fluids, e.g. gravity waves on waver surface¹⁸. Non-classical examples include Kelvin waves on quantized vortex lines¹⁹, gravitational waves (GW)²⁰, waves in fuzzy dark matter²¹ or Bose-Einstein condensates (BEC)²².

Recently, it was suggested that self-similar solutions of the second kind could also prove relevant to describe blow-up condensation scenarios in a class of fourth-order diffusion²², which include as physical examples both the GW and wave turbulence in BEC described by the Nonlinear Schrödinger (NLS) equation. In the case of GW, the relevance of self-similar solutions and anomalous scaling was suggested¹² from the analysis of a companion second-order DAM following the general approach described in Refs.^{11,23}. Construction of relevant second-order DAM is however not necessarily unambiguous: In particular, the reduction strategy from fourth to second order is likely to produce nonphysical results, a feature previously observed in the context of 2D turbulence^{17,24}. Beyond numerical observations and analogies, it remains therefore unclear whether a proper dynamical system analysis can be extended to fourth-order systems, to provide precise characterization of finite-time blow-ups. In the present paper, we study such a finite-time blow-up using numerical simulations of the fourth-order DAM, and characterize its properties in terms of a self-similar Ansatz; This allows to reduce the problem to the analysis of a four-dimensional (4D) dynamical system .

The organisation of the paper is as follows. In Section II, we present a one-parameter family of DAM, which provide fourth-order approximations of the wave kinetic equation for four-wave ($2 \rightarrow 2$) interactions, and prove in particular relevant for GW and waves in the NLS model. Section III focuses on the three-dimensional (3D) GW and the 3D NLS cases; We describe numerical simulations of the evolution problem with compact supported initial spectra, revealing finite time blow-ups at the infrared front, characterized by anomalous spectral exponents. In Section IV, we

discuss the anomalous scaling in terms of simplified second-order DAM and self-similar solutions of the second-kind. In Section V, we extend the approach to the fourth-order case. We characterize the anomalous exponent in terms of a nonlinear eigenvalue problem, and formulate the problem in terms of bifurcation analysis within an autonomous 4D dynamical system. In Section VI, we employ numerical continuation algorithms to explicitly determine the anomalous exponent, in particular for, but not limited to, the 3D GW and the 3D NLS models. Section VII exposes concluding remarks.

II. THE FOURTH-ORDER MODEL

A. The model and notations.

In the present paper, we will study the fourth-order DAM that describes the conservation of the waveaction density (spectrum) $N(\omega, t)$ in frequency space as

$$\partial_t N + \partial_\omega Q = 0, \text{ with } Q(\omega, t) := -\partial_\omega K, \text{ and } K(\omega, t) := \omega^{5-r} N^4 \partial_{\omega\omega}^2 (\omega^r N^{-1}). \quad (1)$$

The coefficient $r = d/\alpha - 1$ is a physical parameter involving the spatial dimension d and the exponent α associated to the dispersion relation of the interacting waves (see next paragraph for examples). The system (1) is a *fourth-order approximation*, as the flux is written as a non-linear Fourier law involving up to the third-derivative of the waveaction spectral density N . The resulting dynamics involves terms up to the fourth derivative of N , hence the name. In previous works, the same equation is sometimes found written in terms of the d -dimensional \mathbf{k} -space waveaction spectrum $n(\mathbf{k}, t)$. The ω -space density is used when the spectrum is isotropic, i.e. independent of the direction of \mathbf{k} ; it relates to the d -dimensional spectrum through integration over the angular directions in \mathbf{k} -space and multiplying by the Jacobian $|\partial k / \partial \omega|$, where the function $\omega(\mathbf{k}, \alpha) \propto k^\alpha$ (with $k = |\mathbf{k}|$) specifies the dispersion relation for the wave frequency in terms of the wave vector length and coefficient α . This gives

$$n(\mathbf{k}, t) \propto \omega^{1-d/\alpha} N(\omega). \quad (2)$$

B. Interpretation: local approximation to kinetic equations.

System (1) describes a one-parameter family of DAM depending upon the coefficient $r := d/\alpha - 1$. The model connects to the four-wave kinetic equation

$$\partial_t n(\mathbf{k}, t) = \int_{\mathbb{R}^{3d}} d\mathbf{k}_* d\mathbf{k}' d\mathbf{k}_*' |T_{\mathbf{k}\mathbf{k}_* \rightarrow \mathbf{k}'\mathbf{k}_*'}|^2 n n' n_* n_*' \left(\frac{1}{n} + \frac{1}{n_*} - \frac{1}{n'} - \frac{1}{n_*'} \right) \delta(\omega + \omega_* - \omega' - \omega_*') \delta(\mathbf{k} + \mathbf{k}_* - \mathbf{k}' - \mathbf{k}_*') \quad (3)$$

with frequency $\omega = k^\alpha$ and interaction coefficient $T_{\mathbf{k}\mathbf{k}_* \rightarrow \mathbf{k}'\mathbf{k}_*'} \equiv T(\mathbf{k}, \mathbf{k}_*, \mathbf{k}', \mathbf{k}_*')$ is a homogeneous function of degree γ : $T(\lambda\mathbf{k}, \lambda\mathbf{k}_*, \lambda\mathbf{k}', \lambda\mathbf{k}_*') = \lambda^\gamma T(\mathbf{k}, \mathbf{k}_*, \mathbf{k}', \mathbf{k}_*')$ for any $\lambda > 0$. Assuming statistical isotropy, $n(\mathbf{k}) \equiv n(k)$, as well as a strong localisation of $T_{\mathbf{k}\mathbf{k}_* \rightarrow \mathbf{k}'\mathbf{k}_*'}$ on neighboring wavenumbers with $\mathbf{k} \approx \mathbf{k}_* \approx \mathbf{k}' \approx \mathbf{k}_*'$, the kinetic equation (3) becomes the slightly generalized two-parameter version of Eq. (1)¹⁶,

$$\partial_t N + \partial_\omega Q = 0, \text{ with } Q(\omega, t) := -\partial_\omega K, \text{ and } K(\omega, t) := \omega^{5-r+2g} N^4 \partial_{\omega\omega}^2 (\omega^r N^{-1}), \quad (4)$$

where $g = \gamma/\alpha$. Then, Eq. (1) is obtained by restricting to the case $g = \gamma = 0$: it is in particular relevant for the GW turbulence in the Einstein vacuum model, as well as the NLS wave turbulence, with application both in nonlinear optics and BEC. Below, we will focus on the systems with $\gamma = g = 0$, but for completeness we present a list of examples including finite g cases in Table I.

System	d	α	γ	r	g
Deep water surface gravity waves ¹⁶	2	$\frac{1}{2}$	3	3	6
Self-gravitating dark matter ²¹	2 or 3	2	-2	0 or $\frac{1}{2}$	-1
Bose-Einstein condensates (NLS) ¹⁶	2 or 3	2	0	0 or $\frac{1}{2}$	0
Gravitational waves in vacuum ^{12,20}	2 or 3	1	0	1 or 2	0

TABLE I. List of relevant parameters in examples of four-wave turbulent systems.

a. Kraichnan-Lee vs Kolmogorov-Zakharov solutions. System (4), which includes System (1) as a special case, is explicitly written in the form of a conservation law for the waveaction N , but it also implies conservation of the energy $E := \omega N$. Indeed, straightforward algebraic

manipulations lead to

$$\partial_t E + \partial_\omega P = 0 \text{ with } P := K + \omega Q. \quad (5)$$

This formulation is naturally equivalent to the formulation of Eq.(4). Yet, one interesting feature of the fourth-order DAM (4,5) is the fact that they truly mimic the physics of dual-cascade systems. At an elementary level, this can be seen from the observation that they feature four different types of pure scaling steady solutions $N \propto \omega^{-x}$. The first types are the equilibrium states with $P = Q = 0$ leading to

$$x = x_N = -r \text{ (Equipartition of } N), \quad \text{or} \quad x = x_E = 1 - r \text{ (Equipartition of } E), \quad (6)$$

respectively. These solutions are asymptotics of a more general Kraichnan-Lee (KL) equilibrium solution $N = \omega^r / (A\omega + B)$ with $A, B = \text{const}$, also known as Rayleigh-Jeans in the wave turbulence literature^{16,25}. The other types are the Kolmogorov-Zakharov (KZ) stationary solutions corresponding to the constant fluxes of energy and waveaction respectively:

$$N = C_P P^{1/3} \omega^{-x_P} \quad \text{and} \quad N = C_Q (-Q)^{1/3} \omega^{-x_Q} \quad (7)$$

with exponents

$$x = x_P = 1 + 2g/3 \text{ (} Q = 0, P \neq 0) \quad \text{and} \quad x = x_Q = \frac{2}{3}(1 + g) \text{ (} Q \neq 0, P = 0) \quad (8)$$

and dimensionless (KZ) constants C_P and C_Q .

The pure direct cascade and the pure inverse cascade power law spectra can in principle be realized only if they correspond to the flux directions $Q < 0$ and $P > 0$ compatible with the standard arguments of the Fjortoft type¹⁶. This condition is satisfied if and only if $2 - 3d/2\alpha < g$ which is true for the GW, the 3D NLS and the deep water gravity waves, but fails for the waves in self-gravitating dark matter and 2D NLS. When this condition fails, the pure cascade states cannot be realised and mixed cascade-thermodynamic (“warm cascade”) states are expected.

Even though the KZ scalings were “built into” the fourth order DAM, the latter have predictive power beyond these scalings and, for instance, give predictions for the constant pre-factors of the KZ spectra¹⁷. Indeed, substituting the two spectra (7) into the expressions of the respective fluxes and taking the ratio of the resulting equations, we get

$$\frac{C_P^3}{C_Q^3} = \frac{(r + 2/3 + 2g/3)(r - 1/3 + 2g/3)}{(r + 1 + 2g/3)(r + 2g/3)}. \quad (9)$$

Note that, to be fully predictive, the right-hand side of the model (4) should contain an order-one pre-factor which depends on a specific wave system. Such a pre-factor however drops out from the ratio C_P/C_Q , and in particular, we get $C_P/C_Q = 0.638$ for the 3D NLS, $C_P/C_Q = 0.905$ for the 3D GW and $C_P/C_Q = 0.970$ for the deep water gravity wave turbulence.

III. NUMERICAL SIMULATIONS OF THE FOURTH-ORDER DAM

In the present work, we restrict our attention to freely evolving wave turbulence (without forcing or/and dissipation). Here, we use the numerical simulations of the fourth-order DAM (1) to characterize the free evolution of an initial condition that features initial compact support around a frequency ω_i in frequency space. Such initial condition has finite energy and waveaction, $\int \omega N d\omega, \int N d\omega < \infty$, and as such, the system could, in principle, propagate the waveaction towards $\omega \rightarrow 0$ through a constant-flux solution, as the corresponding scaling $N \sim \omega^{-2/3}$ entails finite-capacity on the infra-red end, that is $\int_0^{\omega_i} N < \infty$. The compact initial condition cannot, however, sustain a direct cascade towards $\omega \rightarrow \infty$: the latter indeed entails the scaling $N \sim \omega^{-1}$ on the ultra-violet side $\omega \rightarrow \infty$, and this scaling requires an infinite physical space density of waveaction for the spectrum to extend up to $\omega \rightarrow \infty$.

To perform numerics of DAM, it is important to take extra care of the tendency to form sharp propagating fronts with discontinuous derivatives which typically lead to numerical blow-up when a simple differentiation scheme is used. To tackle this obstacle, we rely on smooth noise-robust differentiators, and use a log-discretization in the frequency space to allow for extended computational range. Further technicalities related to our numerical methods are described in Appendix C 1. The numerical results shown in Fig. 1 reveal that the waveaction apparently cascades towards the infra-red end and exhibits scaling close to $2/3$. This corresponds to constant flux solutions, and the direction of the cascade is indeed compatible with the heuristics of Section II. One also observe that the waveaction reaches $\omega \rightarrow 0$ in finite time t_* . For the same initial condition, the blow-up time t_* is ten times smaller in the 3D GW case than in the 3D NLS case, as shown in the insets within the left panels of Fig. 1.

Closer inspection however reveals that those finite-time transients are anomalous: The fluxes converge towards a profile which is not a constant but rather an increasing function of ω , as shown

in the right panels of Fig.1. The compensated spectra shown in Fig. 2 reveal small deviations from pure scaling solutions. Instead of the 2/3 KZ scaling, the numerics feature the behavior $N \sim \omega^{-x_*}$, with $x_* \simeq 0.656$ for the GW and $x_* \simeq 0.659$ for the 3D NLS. In both cases, the deviations to pure KZ scaling is small (1.6% and 1.2% respectively), but measurable. Besides, the infra-red blow-up is algebraic. The front reaches $\omega = 0$ following the apparent power-laws $\propto (t_* - t)^b$ with $b \simeq 3.145$ in the 3D GW case and $b \simeq 3.214$ in the 3D NLS case. The remainder of the paper aims at characterizing such anomalous scalings.

Out of the four-wave systems listed in the table, we choose to study only the GW, the 3D NLS and the systems with $g = 0$, $d = 3$ and $1/2 < \alpha < 9/4$, in particular including the gradual transition from the GW ($\alpha = 1$) to the 3D NLS ($\alpha = 2$) systems. We do not here study the deep water gravitational waves as this system does not have finite capacity at the infra-red end, and therefore does not exhibit an anomalous inverse cascade scaling. Also, we do not study the waves in the self-gravitating dark matter because, as we argued earlier, it has an ordering of the exponents of the stationary power-law solutions inconsistent with the Fjortoft dual cascade argument, meaning that they correspond to a different class in which “warm cascades” are expected.

IV. DEFICIENCY OF THE REDUCTION TO SECOND-ORDER DAM

The anomalous scalings observed in Fig. 2 are reminiscent of behaviors previously observed in second-order DAM^{6,11}. In particular, existence of anomalous transients for the 4th-order DAM for the GW turbulence combined with algebraic finite-time blow-up was suggested from the theoretical and numerical analysis of a companion second-order DAM^{11,26}. Such reduction to second-order DAM can be derived heuristically by engineering the waveaction flux to (i) feature one derivative only, (ii) feature homogeneity $\propto N^3$ as the fourth-order DAM, (iii) yield constant-flux scaling $\propto \omega^{-2/3}$ and (iv) yield equilibrium scaling matching either equipartition of E or N or energy flux. This scheme prescribes the one-parameter family of second-order DAM

$$\partial_t N + \partial_\omega Q = 0 \text{ with } Q := -\omega^{3+\rho} N^2 \partial_\omega N \omega^{-\rho}. \quad (10)$$

By construction, the model has constant flux solution $N \sim \omega^{-2/3}$, and equilibrium solutions $N \sim \omega^\rho$. Constant ρ represents an effective dimension, whose value determines the complimentary equilibrium scaling. The three relevant choices for ρ are $\rho = r$ (waveaction equipartition), $\rho = r - 1$ (energy equipartition) or $\rho = -1$ (constant energy flux). The crucial observation is that

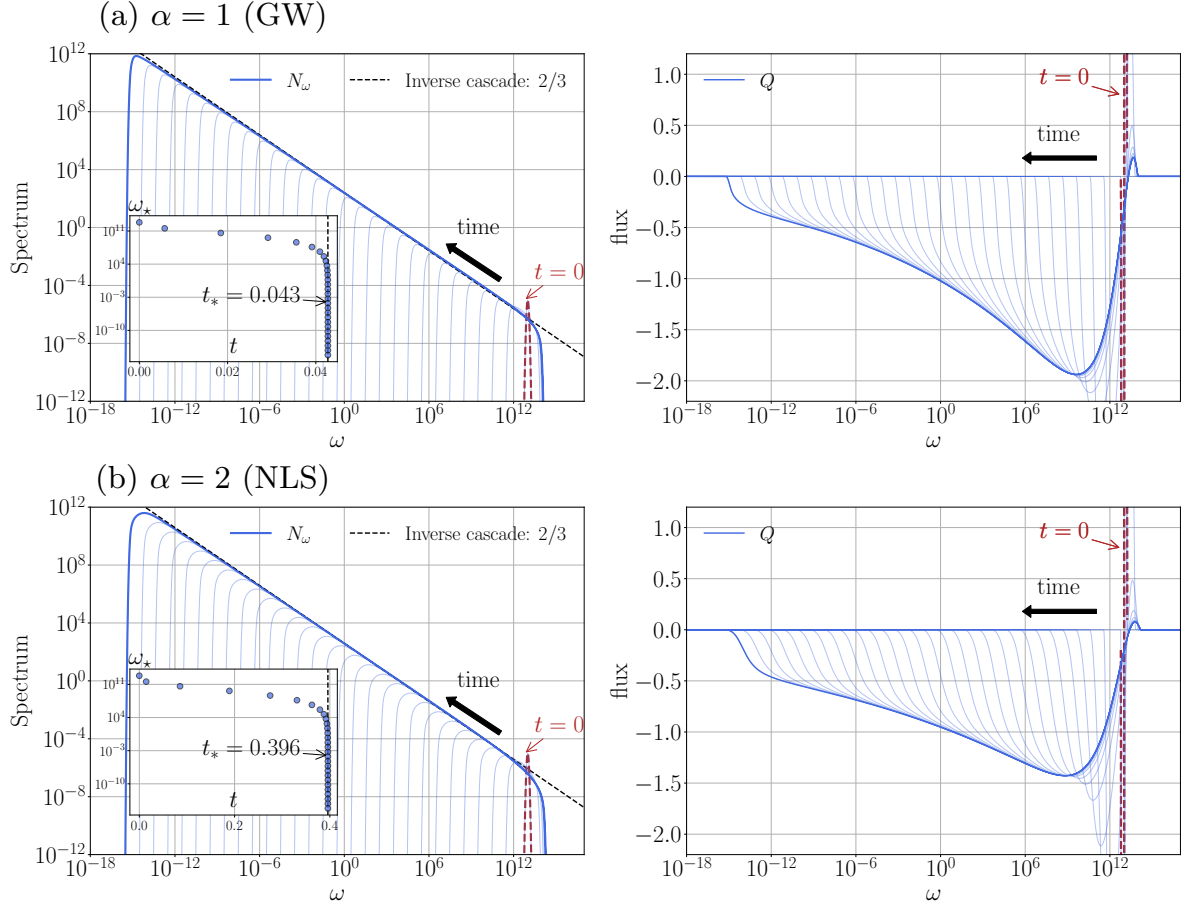


FIG. 1. **Numerical simulations for the fourth-order DAM: spectra and fluxes.** Spectra (left) and fluxes (right) obtained from direct numerical simulations of (a) the 3D GW, and (b) the 3D NLS, starting from the narrow Gaussian profile about $\omega = 10^{12}$ displayed in red. The insets in the left panels show the position of the left front against time, revealing finite-time blow-up. See also videos online.

among those three choices, only the third choice $\rho = -1$ is compatible with inverse cascade of waveaction $N = C\omega^{-2/3}$ with $C > 0$. This comes from the fact that the associated flux is $Q = C^3(\rho + 2/3)$ – negative only provided $\rho < -2/3$. For both the GW and the 3D NLS, the solutions $\rho = r$ and $\rho = r - 1$ do not fulfill this condition. This means that both the GW and the 3D NLS reduce to the same second-order DAM:

$$\partial_t N + \partial_\omega Q = 0, \text{ with } Q := -\omega^2 N^2 \partial_\omega (N\omega). \quad (11)$$

As such, the reduction from fourth to second-order model simplifies the system but cannot explain the weak but measurable difference between the anomalous scalings observed in the GW and the

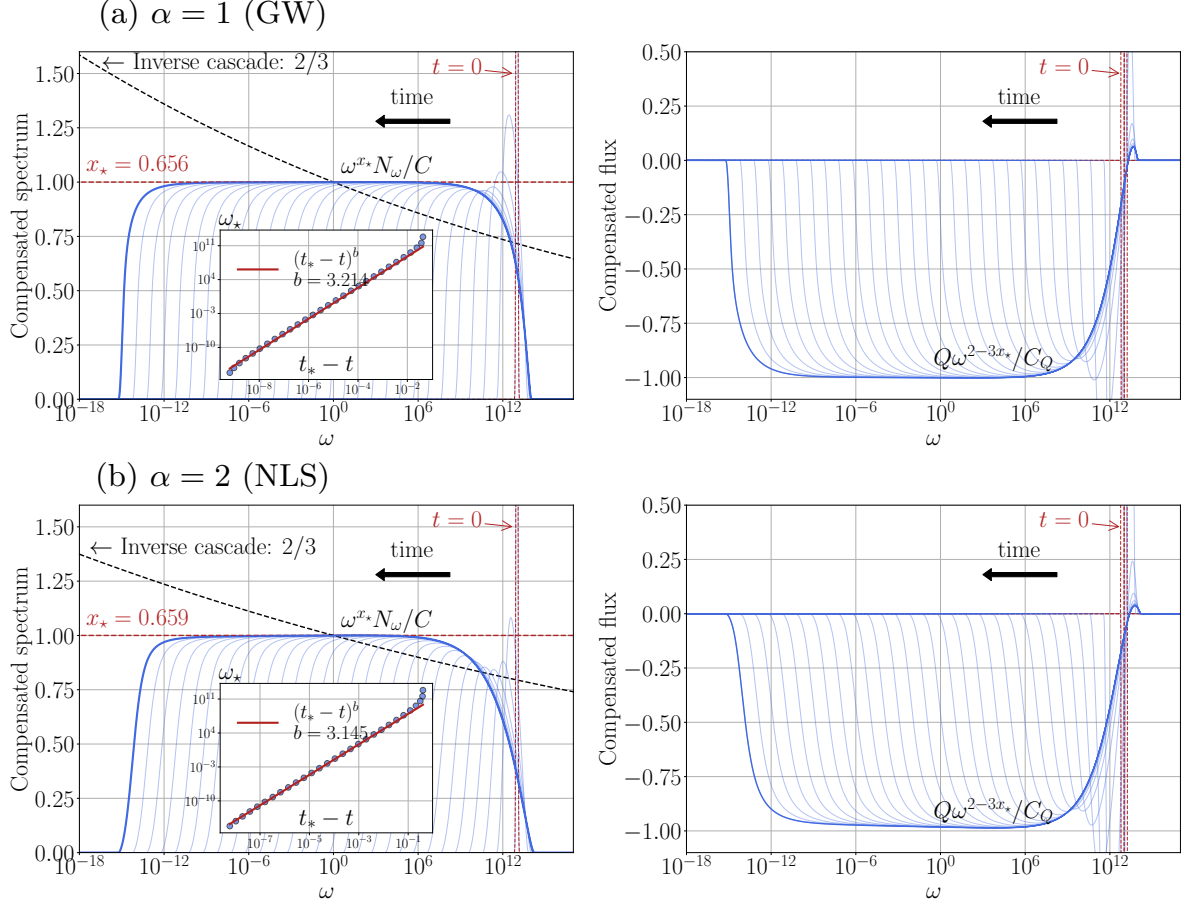


FIG. 2. **Numerical simulations for the fourth-order DAM: compensated spectra and fluxes.** Same as Fig. 1, but this time the spectra and the fluxes are suitably compensated with carefully chosen exponents $x_* \simeq 0.656$ for GW and $x_* \simeq 0.659$ for NLS, and shown in log-lin coordinates. The insets in the left panels show the position of the left front against time $t_* - t$ in log-log coordinates. See also videos online .

3D NLS systems. Indeed, the investigation of Eq.(11) reveals existence of anomalous transients $N \sim \omega^{-x_*}$; the anomalous scaling is $N \sim \omega^{-0.65169}$, only about 2% shallower than KZ, but clearly distinguishable from it in numerics¹². While the anomalous scaling qualitatively matches the observations for the fourth-order DAM, it does not quantitatively correspond to either of the scalings observed in Fig.2. We note that the anomalous scaling in the second-order DAM was previously elucidated¹², and we recall its origin in Appendix A.

Another obvious deficiency of the second-order model is seen at the level of the stationary KZ solutions: One can easily check that the second-order DAM predicts equal values of the KZ constants, *e.g.* $C_P = C_Q$. This is unlike the more realistic fourth-order DAM, which predicts

different values of the KZ constants ($C_P = 0.638C_Q$ for the 3D NLS and $C_P = 0.905C_Q$ for the 3D GW), as seen from Eq. (9). Those undesired deficiencies of the second-order model motivate the detailed investigation of the fourth-order DAM.

V. ANOMALOUS TRANSIENTS AS A SELF-SIMILARITY OF THE SECOND-KIND

A. The nonlinear eigenvalue problem.

We now look for self-similar solutions of the second-kind, which feature a self-similar profile F invading the full infra-red range in finite time $t < t_*$: Introducing the propagating front ω_* and the self-similar variable $\eta := \omega/\omega_*$, those solutions take the form

$$N(\omega, t) = \omega_*^a F(\eta) \quad \text{with} \quad \omega_* \propto (t_* - t)^b, \quad b > 0 \quad (12)$$

and the boundary conditions $F(\eta) \xrightarrow{\eta \rightarrow 1} 0$ “sufficiently smoothly” and $F(\eta) \underset{\eta \rightarrow \infty}{\sim} \eta^{-x}$.

Here, “sufficiently smoothly” means that we select a physically relevant solution such that at the front, where the spectrum vanishes, the fluxes of the waveaction and the energy also vanish (see more about this condition below). The power law asymptotics at the ultra-violet side is an expected feature of self-similar solutions of the second type: finding the power index $x = x_*$ such that the solution satisfies the boundary conditions at both ends constitutes the “nonlinear eigenvalue problem”^{6,11,15,27,28}.

We recall that the coefficient r depends on the physical parameters as $r := d/\alpha - 1$. The condition that $F \sim \eta^{-x}$ must be a valid asymptotic solution for large η requires $a = -x$. The finite-time convergence of the front towards $\omega \rightarrow 0$ requires non-negativity of the coefficient $b > 0$. The specific expression of b is obtained by inserting the Ansatz (12) into the fourth-order system (1) and requiring that the time variable drops out of the resulting equation; this gives

$$b = \frac{1}{2x - 1} > 0. \quad (13)$$

and implies in particular $x > 1/2$. The procedure then also yields the fourth-order ordinary differential equation for F

$$b(xF + \eta \partial_\eta F) = \partial_{\eta\eta} (\eta^{5-r} F^4 \partial_{\eta\eta} (\eta^r F^{-1})) . \quad (14)$$

We define the anomalous value x_* is the exponent x allowing to solve (14) with suitable two-end boundary conditions mentioned above. To specify those in more detail, let us slightly abuse

notations to introduce the self-similar fluxes

$$Q(\eta) := -\partial_\eta K, \quad P(\eta) := K + \eta Q \quad \text{where } K(\eta) := \eta^{5-r} F^4 \partial_{\eta\eta} (\eta^r F^{-1}). \quad (15)$$

Further, let us denote $G = F'$. On the ultraviolet end, algebraic decay $F \sim \eta^{-x}$ prescribes

$$F, G, P, Q \rightarrow 0 \text{ as } \eta \rightarrow \infty. \quad (16)$$

Note also that for $x > 1/2$, scaling solutions $F \sim \eta^{-x}$ the ratio of the r.h.s. of (14) to each of the terms on the l.h.s. asymptotically vanishes as $\eta \rightarrow \infty$, so they are indeed valid asymptotic solutions (see Appendix D 2).

On the infrared end $\eta \rightarrow 1$, we seek solution in form $F \rightarrow C(\eta - 1)^\mu$ for some positive constants C and μ . This expression provides an asymptotic solution of Eq. (14) with vanishing fluxes P and Q if $\mu = 3/2$ and $C = \sqrt{8b/75}$. This can be seen by the direct substitution of such a form into Eq. (14), applying the conditions $P = Q = 0$ at $\eta = 1$, and retaining the leading order in the expansion in small $(\eta - 1)$ (see Appendix D 1). Thus we have

$$F \rightarrow C(\eta - 1)^{3/2}, \quad G \rightarrow \frac{3}{2}C(\eta - 1)^{1/2}, \quad P, Q \rightarrow -\frac{75}{8}C^3(\eta - 1)^{3/2} \quad \text{as } \eta \rightarrow 1. \quad (17)$$

hence implying the sharp front behavior

$$F, G, P, Q \rightarrow 0 \text{ as } \eta \rightarrow 1. \quad (18)$$

B. Reduction to four-dimensional autonomous system.

To analyze solutions of Eq. (14), we now introduce the rescaled variables f, g, p, q , defined through

$$F = f\eta^{-1/2}, \quad F' = g\eta^{-3/2}, \quad P = p\eta^{3/2}, \quad Q = q\eta^{1/2}, \quad (19)$$

which are now considered as functions of the time-like variable $\tau := \log \eta$ ranging from 0 to ∞ .

In terms of the f, g, p, q variables, Eq. (14) becomes the 4D autonomous dynamical system

$$\begin{cases} f'(\tau) = g + \frac{1}{2}f \\ f^2 g'(\tau) = q - p + 2fg^2 + \left(\frac{3}{2} - 2r\right)gf^2 + r(r-1)f^3 \\ p'(\tau) = -\frac{3}{2}p - b(xf + g) \\ q'(\tau) = -\frac{1}{2}q - b(xf + g) \end{cases}, \quad (20)$$

with the primes describing derivatives with respect to the time-like variable τ . The boundary conditions (16)–(18) now become

$$f = g = p = q = 0 \text{ at } \tau = 0, \quad \text{and} \quad f, g, p, q \rightarrow 0 \text{ as } \tau \rightarrow \infty. \quad (21)$$

It is easy to see that the origin $f = g = p = q = 0$ is a fixed point of our dynamical system (see the detailed analysis of the fixed points in Appendix B). In other words, solving Eq. (14) with the specified boundary conditions reduces to searching for a limit cycle passing through the fixed point at the origin, namely a homoclinic cycle. Our conjecture is that such a cycle exists only for a single value of the exponent $x = x_*$: This value leads to a global homoclinic bifurcation, and finding it is the essence of the nonlinear eigenvalue problem at hand. For $x \neq x_*$ no homoclinic trajectory passing through the origin exist: The orbits originating at the origin never return to the origin. Since the homoclinic cycles have infinite time periods and since they are realised for $x = x_*$, we will later refer to such cycles as ∞_* -cycles.

VI. CHASING THE ∞_* -CYCLES

A. The ∞_* -cycles in the second-order models.

The idea of solving the nonlinear eigenvalue problem by connecting its solution to the presence of a global bifurcation in a suitable associated autonomous dynamical system was previously done for the second-order DAM^{11,15}, including but not limited to Leith's original model. The following scenario was then discovered: When changing the parameter x , one first observes change of stability of an isolated fixed point resulting in the creation of a limit cycle through a Hopf bifurcation. As x is further varied, such a cycle grows until it simultaneously collides at with two isolated fixed points, one for each boundary conditions. In technical words, this scenario is that of a global bifurcation giving birth to a heteroclinic cycle, namely an ∞_* cycle composed of two heteroclinic orbits. One of the orbits is the solution of the nonlinear eigenvalue problem, and this determines x_* . Solving the nonlinear eigenvalue problem for the second-order DAM therefore also boils down to chasing an ∞_* -cycle; The property that the global bifurcation creates a heteroclinic cycle rather than a homoclinic one is not universal, and merely depends on the choice of reduced variables.²⁹ The bifurcation theory for 2D dynamical systems guarantees the existence and the uniqueness of

the global bifurcation. While x_* cannot be determined analytically, the theory provides bounds for its value, which has to be smaller than the Hopf value x_H and greater than the KZ exponent^{15,30}.

B. The ∞_* -cycles in the fourth-order models.

a. Methods. Our aim is to identify the ∞_* -cycles for the one-parametric family of fourth-order DAM and associated 4D dynamical system (20), obtained by varying the coefficient $\alpha \in [0.5, 2.25]$, with the other parameters $g = 0, d = 3$ prescribed as in the 3D NLS and the 3D GW systems; see Table I. Bifurcation theory being less exhaustive for dynamical systems in 4D than in 2D, we therefore rely on several additional tools to identify the ∞_* -cycles arising in the 4D system (20): In addition to the local analysis described in Appendix B, our description uses the classification of co-dimension 1 bifurcations of limit cycles, as well as numerical continuation algorithms and the Simpson strategy described in Appendix C 2.

Unlike 2D, where limit cycles are found to possess stable direction in reverse time, the limit cycles in 4D have unstable directions in both forward and reverse time. As such, only a set of initial conditions with zero-measure results in trajectories attracted to the cycles. This motivates the use of numerical continuation algorithms rather than shooting methods, in order to identify and track the cycles. We specifically rely on the PyCont software from the PyDSTool library³¹.

b. Generic vs non-generic cases. The main outcome of our analysis is the conjecture that similar to the 2D case, there exists a unique global bifurcation for each member of our α -parametric family of 4D models, each time leading to the creation of an ∞_* -cycle at some prescribed value of x_* . Due to our specific choice of variables f, g, p, q , the ∞_* -cycle stems from a homoclinic bifurcation. The specific scenarios leading to such global bifurcation however depend on the 4D system being or not *generic*.

1. *Generic systems* are obtained for $\alpha < 2$, or alternatively $r > 1/2$, in which case the reduced system (20) possesses two isolated fixed points, namely the origin and a point P_+ , which undergoes a Hopf bifurcation for some value $x = x_H$. This includes the GW system. Cycles are found to exist only in between the Hopf value and the KZ value $x_Q = 2/3$, hereby bounding the value of x_* as in the 2D case.
2. *Non-generic systems* are obtained for $\alpha \geq 2$, or alternatively $r \leq 1/2$: No isolated fixed point exist except for the origin. Cycles then exist only for values of x in between the energy

equipartition exponent $1 - r$ and the KZ exponent $2/3$, thereby altering the bounds for x_* compared to the 2D case. The NLS system is the critical case $\alpha = 2$, for which the Hopf value collides with the equipartition exponent $x_E = 1 - r$; see Fig. 5. When approaching the NLS system from below, *e.g.* $\alpha \rightarrow 2^-$, the isolated fixed point P_+ moves to ∞ ; see the green lines in Panels (a) of Fig. 5 and 7.

c. Basic classification of co-dimension 1 bifurcations. In both the generic and the non-generic cases previously described, we expect the ∞_* -cycle to emerge out of a series of co-dimension 1 bifurcations of limit cycles, which can be tracked down all the way either from infinity or from the Hopf point, provided the latter exists. Following the general classification of co-dimension 1 bifurcations³², those can either correspond to *flip*, *fold* or *torus* bifurcations³². As a very brief reminder, we here simply recall that a flip bifurcation of limit cycles generically indicates a period doubling (PD), *i.e.* a cycle emerges with twice the period of the original cycle, while the original cycle changes its stability. A fold bifurcation of limit cycles generically corresponds to a turning point of a *curve of limit cycles*, known as a limit point of cycle (LPC), and characterized by either the birth or the mutual annihilation of two cycles with different stability. The curve of limit cycles may be defined from any relevant feature of the cycles. Here, we track either the minimal or the maximal value of the variable f on the cycles with respect to x ³², as seen in Panels (a) of Fig. 3 & 4. Finally, the torus (Neimark-Sacker) bifurcation of limit cycles generically corresponds to a bifurcation of a cycle to an invariant torus, on which the flow contains periodic or quasi-periodic motions.

C. Generic and non-generic routes towards the ∞_* -cycle.

We now describe in more details the two bifurcation scenarios leading to the global bifurcation for the GW (generic) and the NLS (degenerate) cases. Unlike in 2D, where there is one and only one limit cycle present for the values of x in between of x_H and x_* (see Fig. 6 in Appendix A), a wider variety of scenarios occurs in 4D, with limiting cycles emerging or disappearing for values in between x_H and x_* , or cycles existing for $x > x_*$.

a. Bifurcations towards the GW ∞_ - cycle.* The curves presented in Fig.3 show the bifurcations of limit cycles leading to the ∞_* -cycle relevant in the GW case $\alpha = 1$. It is obtained by performing the numerical continuation initialized at $x = x_H \approx 0.600$, where a (small) limit cycle emerges. Panel (a) tracks the maximal and the minimal values of $f(\tau)$ encountered on the cycles

when varying the parameter x . The corresponding periods are shown in Panel (b). The leftmost (green) point in Panel (a) corresponds to the Hopf bifurcation, while the pair of red dots closest at $x \approx 0.605$ features the birth of a small cycle; Its 3D projection onto the space (f, p, q) is shown in Panel (c). Increasing x , a fold bifurcation occurs at $x \approx 0.636$ giving birth to two more cycles; This event is signaled by the second pair of red dots on the vertical dashed line at $x \approx 0.636$ in Panel (a); As x is increased, the two new cycles separate from each other, emerging out of the red cycle featured in Panel (d). Note that the cycle directly branching from the Hopf bifurcation continues to exist: It is represented both by the pair of white dots in Panel (a) at $x \approx 0.636$, and the blue curve in Panel (d). Further increasing x , four further fold bifurcations occur, leading to creation or annihilation of pairs of cycles. In particular, the cycles branching from the Hopf point eventually vanishes by colliding with another remaining cycle at some $x \simeq 0.66 > x_*$, and no cycles exist in the system for greater values of x . In this scenario, a unique ∞_* - cycle appears at $x = x_* = 0.656$, and is the red one in Panel (e). It is the outcome of a homoclinic bifurcation, with one of the cycle originating from the ultimate fold bifurcation colliding with the origin.

b. Bifurcations towards the NLS ∞_ - cycle.* The 3D NLS system with $\alpha = 2$ is a degenerate system for which the isolated fixed point P_+ has escaped to infinity. The continuation algorithm then cannot be properly initiated from the Hopf point; To construct the bifurcation diagram at fixed $\alpha = 2$, we rely on the Simpson strategy described in Appendix C 2. In brief, the strategy consists in generating various co-dimension 2 continuation curves branching from randomly selected points on the continuation curve $\alpha = 1, x = x_1$ to $\alpha = 2, x = x_2$. This initializes the continuation algorithms on various random branches on the plane $\alpha = 2$, rather than on the degenerate Hopf point. The outcome of the process is represented in Fig. 4. The bifurcation diagram is plotted in Panel (a) and the respective periods in Panel (b) of Fig.4. Panels (c), (d) and (e) show the 3D projections of the cycles for the values of x marked by the red and white dots in the previous panels. The Hopf cycle emanating from infinity corresponds to a periodic orbit of infinite amplitude in the limit $x \rightarrow 0.5^+$. From the Hopf point, the diagram features a sequence of fold bifurcations, occurring at various values of x . While more intricate, this scenario remains qualitatively similar to the generic example represented by the 3D GW case. However, the NLS bifurcation scenario has also a series of distinctive features. First, as seen in Panel (d), the cycles emerging from the first three fold bifurcations have rather intricate structure featuring up to seven loops; Panel (d) shows the already complicated pattern at $x \simeq 0.551$ where three cycles exist together. Second, in addition to the folds we observe a flip bifurcation, represented by the green dots in Panels (a)

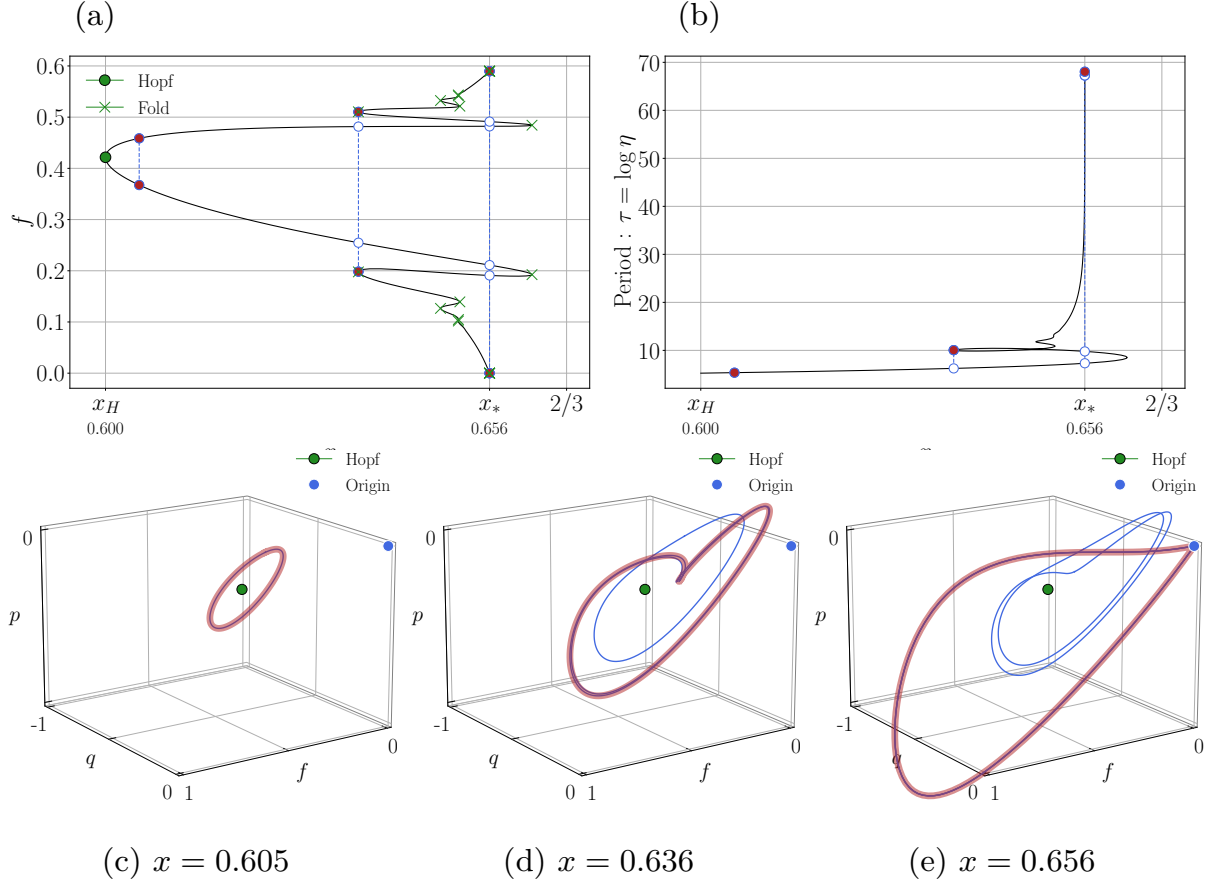


FIG. 3. **Periodic solutions in the 3D GW case.** Panel (a) tracks the cycles by showing the minima and maxima of the profiles $f(\tau)$. Panel (b) shows the corresponding periods. Panels (c,d,e) show 3D projections of the cycles found at different x , indicated by the white and red dots in the previous panels (white dots–blue cycles, red dots–red cycles). The ∞_* -cycle (in red) is found at $x_* \simeq 0.656$.

and (b) at $x \approx 0.595$: The cycle branching from the Hopf bifurcation then changes its stability. Besides, Panel (b) shows clearly that the new cycle emerging at $x \approx 0.595$ has a period twice the original cycle marked by the green dot. Third, in addition to x_* , there are four more values of x at which the cycle periods turn very large (possibly infinite). These cycles are not ∞_* -cycles because they remain at finite distance from the origin, *e.g.* f_{\min} remains finite, as explicit in Panel (a). Still, such cycles are very large in the 4D phase space, with in particular $f_{\max} \rightarrow \infty$; see also Panel (a) of Fig. 7.

A closer inspection (not shown here) reveals that pieces of those spurious giant cycles follow the line $(f, -f/2, -f/3, -f)$; On this line, the 4D system satisfies $\dot{f} = \dot{p} = \dot{q} = 0$ and $\dot{g} = -2/(3f) \rightarrow 0$ as $f \rightarrow \infty$, meaning that the giant cycles indicate degenerate homoclinic

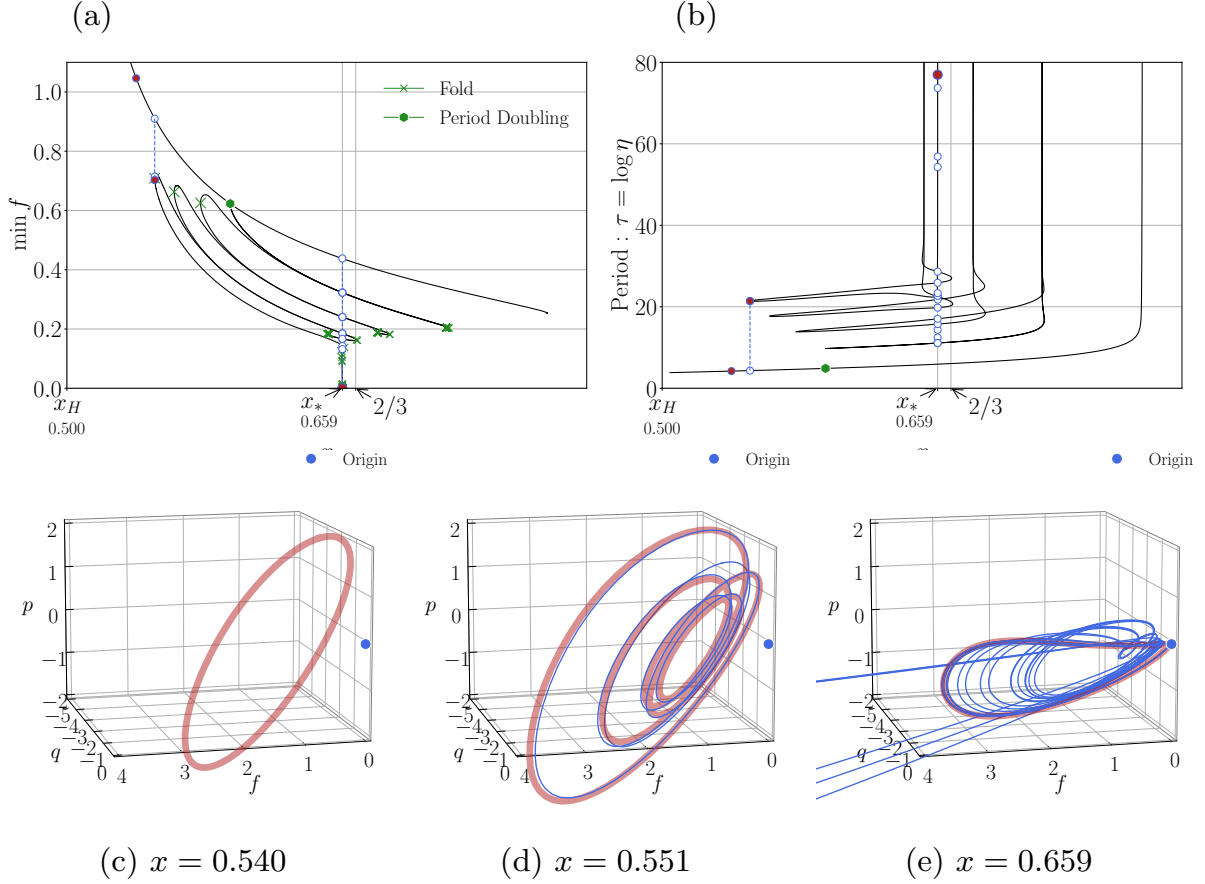


FIG. 4. **Periodic solutions in the 3D NLS case.** Panel (a) tracks the cycles by showing the minima of $f(\tau)$. Panel (b) shows the corresponding periods. Panels (c,d,e) show 3D projections of the cycles found at different values of x , indicated by the white and red dots in the previous panels. The ∞_* -cycle shown in red in Panel (e) is found at $x_* \simeq 0.659$.

bifurcations, featuring the collision of a cycle with a fixed point P_+ at infinity. Fourth, unlike the GW case, there exists a great, possibly infinite, number of folds occurring in the small vicinity of the value $x = x_* \approx 0.659$ for which the ∞_* -cycle emerges; This is signaled in Panel (e) by the numerous cycles in blues, apparently arbitrarily close to the ∞_* -cycle (red). As an aside, we note that for the cases $\alpha > 2$ or equivalently $r < 1/2$, the point P_+ does not exist, but the bifurcation diagram is qualitatively similar to the one of the singular 3D NLS case with $\alpha = 2$. In particular, the giant cycles containing straight line segments continue to exist, as well as the very large number of folds arbitrarily close to x_* .

D. The ∞_* - cycle in the general case: observations and conjectures.

To reveal general properties of the self-similar solutions of the second kind for both generic and non-generic fourth-order systems, we now compute the continuation curve varying parameter α from 0.50 to 2.25 and x from 0.5 to 2.25, hereby directly tracking the ∞_* - cycles. In practice, this co-dimension 2 continuation is initialized from the ∞_* - cycles at $\alpha = 1$. Our findings are summarised in Fig. 5. Panel (a) shows the behavior of the exponents x_H and x_* as a function of α , comparing it to the energy equipartition exponent $x_E(\alpha) = 2 - d/\alpha$, as well as the KZ of exponent $x_Q = 2/3$ for the stationary inverse cascade KZ spectrum. Note that the Hopf point and the energy equipartition coincide at $\alpha = 2$, *e.g.* $x_H = x_E$; At $\alpha = 2.25$, three exponents coincide, namely $x_E = x_Q = x_*$. Panels (b) and (c) show 2D projections on which the ∞_* -cycles are overlaid with the orbits obtained by numerical simulations of the respective fourth-order differential equation showing the evolving spectra arising for finite-support initial data. Agreement between the profiles is excellent, and this confirms that the value of x_* determined by numerical continuation is indeed the one relevant for the second-kind self-similarity.

Based on the information presented in Fig.5, we propose the following conjectures:

- (i) x_* exists and is unique for all $r > 1/3$;
- (ii) x_* is bounded: $\min(x_H, x_E = 1 - r) < x_* < x_Q = 2/3$;
- (iii) $x_* \rightarrow x_Q = 2/3$ as $r \rightarrow 1/3$. In this limit, the energy equipartition exponent x_E coincides with the one of inverse cascade KZ, x_Q . This should correspond to the finite-time blow-up becoming infinite, *i.e.* $t_* \rightarrow \infty$;
- (iv) The ∞_* -cycles represent stable self-similar solutions of the second kind which are attractors for the spectra evolving out of finite-support initial data of arbitrary shape.

VII. CONCLUDING REMARKS

Using numerical simulations and a self-similarity Ansatz, we have shown the existence of anomalous transients in the inverse cascade of fourth-order DAM (1) relevant for a class of wave-turbulence systems. We focused on a continuous one-parametric class of systems which includes the 3D GW and the 3D NLS as special cases. Such anomalous transients are mis-characterized in second-order DAM, which fail to distinguish between the 3D GW and the 3D NLS cases. By

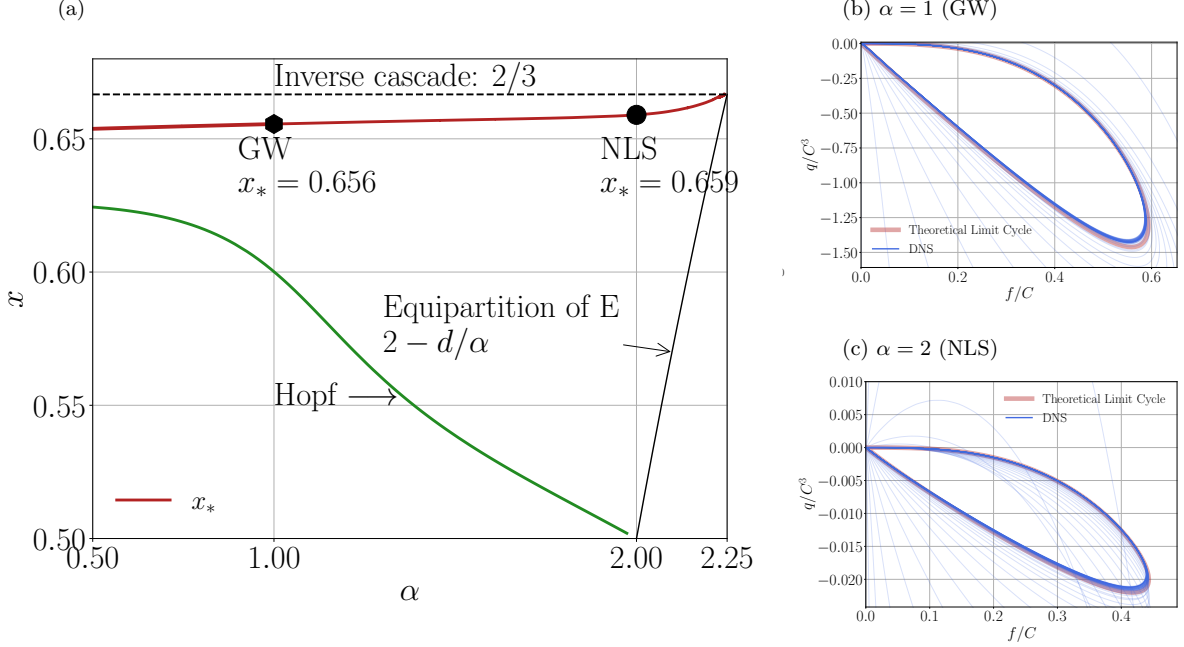


FIG. 5. **Full phase portrait.** Panel (a) shows the various scaling exponents as a function of α and fixed $d = 3$. The line of anomalous exponent x_* is the practical outcome of our analysis. Panels (b,c) compare the ∞_* -cycles with the DNS profiles reported in Fig.2. The fine blue lines are transients before the simulation adjusts to self-similar profile of the second-kind. See also videos online .

taking into account the correct interplay between KL and KZ solutions, the fourth-order DAM are found to feature weak but non-trivial systematic deviations between the anomalous transients and the KZ solutions. From careful numerical simulations, we have identified the presence of anomalous scaling, and observed that the deviations to KZ scaling are very small, less than 1% for both the 3D GW and the 3D NLS cases. Those transients can be precisely related to convergence of the solutions to self-similar solution of the second-kind featuring finite-time blow-up of the propagating front, and this is our main result. This characterization allows for a very precise determination of the exponent and of the self-similar profile using the theory of dynamical systems. We provided a systematic way of determining the anomalous transients. To that end, we extended and reformulated a previous analysis of self-similarity of the second kind in second-order DAM, to relate x_* to the existence of an ∞_* -cycle. Rather than direct computations of trajectories of the associated dynamical system, *e.g.* using shooting methods which in the present case prove highly inefficient, we relied on numerical continuation software, to chase and identify the cycle in the 4D phase space. This is, to our knowledge, the only efficient way of determining the exponent

x_* . Agreement with the numerical simulations is found to be excellent, proving that the found self-similar solutions are stable: They represent the large-time asymptotics for spectra evolving out of finite-support initial data of arbitrary shape. Our findings about the self-similar transients are summarised as a set of four conjectures in the end of the previous section.

Among natural perspectives for this work is the full classification of the self-similar transients in a wider class of fourth-order DAM given by Eq. (4), as well as extending the description by including the finite-capacity direct cascades³³. In particular, it would be useful to include the important example of the gravity wave turbulence on the deep water surface. Even more challenging but important task would be to extend our approach to the integro-differential wave-kinetic equations which are more realistic in describing wave turbulence than the differential models considered in the present article. In the same spirit, it would also be interesting to study other integro-differential closures, possibly including turbulent systems with spectra varying in both the wave number and the physical space, *e.g.*, non-Markovian Liouville equation suggested in Refs.^{34,35} for the plasma drift waves.

ACKNOWLEDGEMENTS

The authors thank A. Mailybaev for useful discussions. ST acknowledges support from the Programa de Capacitação Institucional of CNPq and the French-Brazilian network in mathematics. The work of VG was partially supported by the “chercheurs invités” awards of the Fédération Doeblin FR 2800, Université de la Côte d’Azur, France. The work of SN was supported by the Chaire D’Excellence IDEX (Initiative of Excellence) awarded by Université de la Côte d’Azur, France, Simons Foundation Collaboration grant Wave Turbulence (Award ID 651471), the European Unions Horizon 2020 research and innovation programme in the framework of Marie Skłodowska-Curie HALT project (grant agreement No 823937) and the FET Flagships PhoQuS project (grant agreement No 820392). The work of SM was supported by state funding program FSUS-2020-0034.

References

1. C. Leith, “Diffusion approximation to inertial energy transfer in isotropic turbulence,” *The Physics of Fluids* **10**, 1409–1416 (1967).
2. T. Lee, “On some statistical properties of hydrodynamical and magneto-hydrodynamical fields,” *Quarterly of Applied Mathematics* **10**, 69–74 (1952).

3. R. Rubinstein, T. Clark, and S. Kurien, “Leith diffusion model for homogeneous anisotropic turbulence,” *Computers & Fluids* **151**, 108–114 (2017).
4. T. Clark, R. Rubinstein, and J. Weinstock, “Reassessment of the classical turbulence closures: the Leith diffusion model,” *Journal of Turbulence* , N35 (2009).
5. S. Orszag and D. Raila, “Test of spectral energy transfer models of turbulence decay,” *The Physics of Fluids* **16**, 172–173 (1973).
6. C. Connaughton and S. Nazarenko, “Warm cascades and anomalous scaling in a diffusion model of turbulence,” *Physical review letters* **92**, 044501 (2004).
7. D. K. Lilly, “Two-dimensional turbulence generated by energy sources at two scales,” *Journal of Atmospheric Sciences* **46**, 2026 – 2030 (1989).
8. P. Morel, S. Xu, and O. D. Gurcan, “A differential approximation model for passive scalar turbulence,” *Journal of Physics A: Mathematical and Theoretical* **54**, 335701 (2021).
9. V. L’vov, S. V. Nazarenko, and G. Volovik, “Energy spectra of developed superfluid turbulence,” *Jetp Lett.* **80**, 479–483 (2004).
10. V. L’vov, S. V. Nazarenko, and L. Skrbek, “Energy spectra of developed turbulence in helium superfluids,” *J Low Temp Phys* **145**, 125–142 (2006).
11. S. Thalabard, S. Nazarenko, S. Galtier, and S. Medvedev, “Anomalous spectral laws in differential models of turbulence,” *Journal of Physics A: Mathematical and Theoretical* **48**, 285501 (2015).
12. S. Galtier, E. Nazarenko, S. and Buchlin, and S. Thalabard, “Nonlinear diffusion models for gravitational wave turbulence,” *Physica D: Nonlinear Phenomena* **390**, 84–88 (2019).
13. V. L’vov, E. Podivilov, A. Pomyalov, I. Procaccia, and D. Vandembroucq, “Improved shell model of turbulence,” *Physical Review E* **58**, 1811 (1998).
14. C. Campolina and A. Mailybaev, “Chaotic blowup in the 3D incompressible Euler equations on a logarithmic lattice,” *Physical review letters* **121**, 064501 (2018).
15. V. Grebenev, S. Nazarenko, S. Medvedev, Y. Chirkunov, and I. Schwab, “Self-similar solution in Leith model of turbulence: anomalous power law and asymptotic analysis,” *Journal of Physics A: Mathematical and Theoretical* **47**, 025401 (2014).
16. S. Nazarenko, *Wave turbulence*, Vol. 825 (Springer Science & Business Media, 2011).
17. V. L’vov and S. Nazarenko, “Differential model for 2D turbulence,” *JETP letters* **83**, 541–545 (2006).
18. S. Hasselmann, K. Hasselmann, J. H. Allender, and T. P. Barnett, “Computations and parameterizations of the nonlinear energy transfer in a gravity-wave spectrum. part ii: Parameterizations of the nonlinear energy transfer

- for application in wave models,” *Journal of Physical Oceanography* **15**, 1378 – 1391 (1985).
19. S. Nazarenko, “Differential approximation for kelvin wave turbulence,” *Jetp Lett.* **83**, 198–200 (2006).
 20. S. Galtier and S. Nazarenko, “Turbulence of weak gravitational waves in the early universe,” *Physical Review Letters* **119**, 221101 (2017).
 21. V. Skipp, J. and L’vov and S. Nazarenko, “Wave turbulence in self-gravitating Bose gases and nonlocal nonlinear optics,” *Physical Review A* **102**, 043318 (2020).
 22. C. Connaughton and Y. Pomeau, “Kinetic theory and Bose–Einstein condensation,” *Comptes Rendus Physique* **5**, 91–106 (2004).
 23. S. Nazarenko and V. Grebenev, “Self-similar formation of the Kolmogorov spectrum in the Leith model of turbulence,” *Journal of Physics A: Mathematical and Theoretical* **50**, 035501 (2016).
 24. C. Leith, “Diffusion approximation for two-dimensional turbulence,” *The Physics of Fluids* **11**, 671–672 (1968).
 25. R. Kraichnan, “Inertial ranges in two-dimensional turbulence,” *The Physics of Fluids* **10**, 1417–1423 (1967).
 26. S. Nazarenko, V. Grebenev, S. Medvedev, and S. Galtier, “The focusing problem for the Leith model of turbulence: a self-similar solution of the third kind,” *Journal of Physics A: Mathematical and Theoretical* **52**, 155501 (2019).
 27. N. Bell, V. Grebenev, S. Medvedev, and S. Nazarenko, “Self-similar evolution of alfven wave turbulence,” *Journal of Physics A: Mathematical and Theoretical* **50**, 435501 (2017).
 28. B. Semisalov, V. Grebenev, S. Medvedev, and S. Nazarenko, “Numerical analysis of a self-similar turbulent flow in bose–einstein condensates,” *Communications in Nonlinear Science and Numerical Simulation* **102**, 105903 (2021).
 29. In Appendix A, we show that upon using variables akin to f, g, p, q variables which we introduced to address the fourth-order DAM, the global bifurcation which determines x_* for the second-order DAM describes the appearance of a homoclinic cycle.
 30. V. N. Grebenev, S. V. Nazarenko, and S. B. Medvedev, “Complementary remarks to properties of the energy spectrum in leith’s model of turbulence,” *ZAMM - Journal of Applied Mathematics and Mechanics / Zeitschrift für Angewandte Mathematik und Mechanik* **97**, 664–669 (2017), <https://onlinelibrary.wiley.com/doi/pdf/10.1002/zamm.201600060>.
 31. W. Clewley, R. and Sherwood, M. LaMar, and G. J., “PyDSTool, a software environment for dynamical systems modeling,” <http://pydstool.sourceforge.net> (2007), [Online; accessed 18-January-2021].
 32. Y. Kuznetsov, *Elements of applied bifurcation theory*, Vol. 112 (Springer Science & Business Media, 2013).
 33. C. Connaughton, A. Newell, and Y. Pomeau, “Non-stationary spectra of local wave turbulence,” *Physica D*:

- Nonlinear Phenomena **184**, 64–85 (2003).
34. R. Balescu, “Drift-wave turbulence and zonal flow generation,” *Phys. Rev. E* **68**, 046409 (2003).
 35. R. Balescu, I. Petrisor, and M. Negrea, “Anisotropic electrostatic turbulence and zonal flow generation,” *Plasma Physics and Controlled Fusion* **47**, 2145–2159 (2005).
 36. F. R. Gantmacher and J. L. Brenner, *Applications of the Theory of Matrices* (Courier Corporation, 2005).
 37. B. D. Hassard, N. D. Kazarinoff, and Y.-H. Wan, *applications of Hopf bifurcation*, Vol. 41 (CUP, 1981).
 38. P. Holoborodko, “Smooth noise-robust differentiators,” accessed 01/19/2021 (2015).
 39. G. Van Rossum and F. Drake, *Python 3 Reference Manual* (CreateSpace, Scotts Valley, CA, 2009).
 40. P. Peterson, “F2PY: a tool for connecting Fortran and Python programs,” *International Journal of Computational Science and Engineering* **4**, 296–305 (2009).
 41. J. Simpson, *Touching the Void* (Harper Perennial, 1988).

Appendix A: Dynamical system analysis for the second order DAM: digest

a. Self-similar solution of the second kind. The second-order DAM introduced in section IV is the conservation law

$$\partial_t N + \partial_\omega Q = 0, \text{ with } Q := -\omega^{3+\rho} N^2 \partial_\omega (\omega^{-\rho} N). \quad (\text{A1})$$

Pure scaling stationary solutions are either the equilibrium solutions $N \sim \omega^\rho$ or the cascade KZ solution $N = (3Q/(3\rho - 2))^{1/3} \omega^{-2/3}$. Inverse cascade solutions require $Q < 0$ and, therefore, $\rho < 2/3$.

For $\rho = -1$, Eq. (A1) has an equilibrium solution with the scaling $N \sim \omega^{-1}$: This scaling coincides with that of the direct cascade solution of the fourth-order DAM, for both the 3D GW and the 3D NLS (and in fact all the admissible models with $\gamma = 0$).

We look for a self-similar solution of the second-kind describing finite-time infrared blow-up. Writing

$$N(t, \omega) = \omega_*^{-x} F(\eta), \text{ with } \eta = \omega/\omega_*, \omega_* \sim (t_* - t)^b, \text{ and } b := \frac{1}{2x - 1} \quad (\text{A2})$$

yields the second-order ODE, in terms of the self-similar profile F and the self-similar flux Q

$$\begin{cases} \partial_\eta F = -Q\eta^{-3} F^{-2} + \rho\eta^{-1} F \\ \partial_\eta Q = b((x - \rho)F + Q\eta^{-2} F^{-2}) \end{cases}, \text{ with boundary conditions } F = Q = 0 \text{ at } \eta = 1 \text{ and } \eta \rightarrow \infty. \quad (\text{A3})$$

b. Reduction to an autonomous system. The system can be reduced to a second-order autonomous system, in terms of the parametrization $\tau = \log \eta$ and the rescaled variables $f = \eta^{1/2} F$ and $q = \eta^{-1/2} Q$, as

$$\begin{cases} f'(\tau) = (\rho + \frac{1}{2}) f - q f^{-2}, \\ q'(\tau) = -\frac{1}{2} q + b (q f^{-2} - (\rho + x) f) \end{cases} \quad (\text{A4})$$

with boundary conditions $f = q = 0$ at $\tau = 0$ and $\tau \rightarrow \infty$. To remove singularity at the origin, one can rely on the parametrization $\theta := \int_1^\tau f^{-2} d\tau'$, and obtain the system

$$\begin{cases} f'(\theta) = (\rho + \frac{1}{2}) f^3 - q, \\ q'(\theta) = -\frac{1}{2} q f^2 + b (q - (\rho + x) f^3) \end{cases} \quad (\text{A5})$$

c. The ∞_ -cycle.* A unique solution to system (A4) exists for a unique value of the exponent $x < 2/3$, as proven in a more general case²³. In previous works^{11,12}, the specific value of x was found using the shooting methods and a different set of rescaled variables instead of the variables f, q . Here, we rely on the numerical continuation algorithms provided by the Python library PyDSTool³¹ to retrieve those results. We observe that for $\rho < -1/2$, the system has three fixed points, namely the marginally stable node $(f, q) = (0, 0)$ and the foci $(f_\pm, q_\pm) = \pm(-1/2 - \rho)^{-1/2}, -(-1/2 - \rho)^{-3/2}$.

The positive focus (f_+, q_+) undergoes Hopf bifurcation at $x_H \simeq 0.6250$, and gives rise to a branch of stable periodic orbits. Fig. 6 shows the outcome of the continuation algorithm; the left panel shows that the branch of periodic solutions stops at $x = x_* \simeq 0.6517$, at which point the cycle collides with the marginal node $(0, 0)$. Besides, the right panel shows that the final cycle has infinite period: $x_* \simeq 0.6517$ is therefore the looked-after exponent, as indeed previously found from the shooting methods¹².

Appendix B: Fixed point analysis and Hopf bifurcation.

The system (20) is singular at the origin $f = g = p = q = 0$. To apply the standard fixed-point analysis, we remove the singularity by changing the time variable $\tau \rightarrow \theta = \int_{\tau_0}^\tau f^{-2}(\tau') d\tau'$ (with

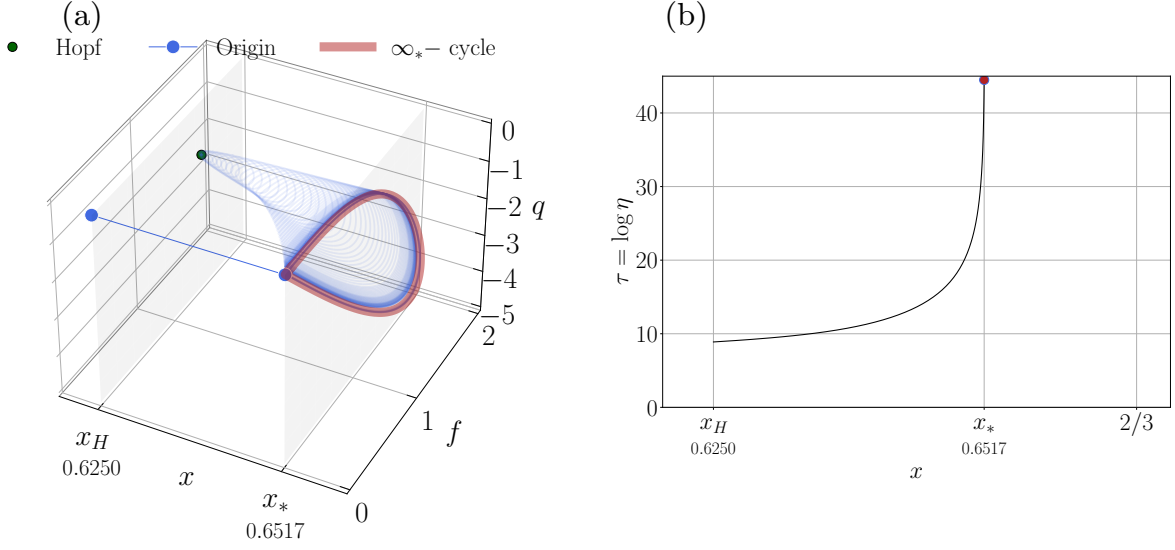


FIG. 6. **Numerical continuation for the second-order DAM.** Panel (a): the periodic orbits of system (A4) growing from the Hopf point at $x = x_H$ to the point x_* where it collides with the marginal node $(0, 0)$. The final homoclinic orbit is shown in red. Panel (b) shows the period of the cycles as a function of x .

arbitrary $\tau_0 > 0$) thereby obtaining the following system,

$$\begin{cases} f'(\theta) = f^2 \left(g + \frac{1}{2}f \right), \\ g'(\theta) = q - p + 2fg^2 + \left(\frac{3}{2} - 2r \right) gf^2 + r(r-1)f^3, \\ p'(\theta) = -f^2 \left(\frac{3}{2}p + b(xf + g) \right), \\ q'(\theta) = -f^2 \left(\frac{1}{2}q + b(xf + g) \right). \end{cases} \quad (\text{B1})$$

System (B1) admits a 2D stationary manifold $\mathcal{S} = \{(f, g, p, q) \in \mathbb{R}^4 : f = 0, p = q\}$ on which the points have marginal stability. Indeed, consider small deviations from a point on the stationary manifold \mathcal{S} , i.e., $f = \tilde{f}$, $g = g_0 + \tilde{g}$, $p = q_0 + \tilde{p}$, $q = q_0 + \tilde{q}$.

In terms of the variable $y = 2g_0^2 f + \tilde{p} - \tilde{q}$, System (B1) becomes

$$\begin{cases} f'(\theta) = f^2 \left((g_0 + \tilde{g}) + \frac{1}{2}f \right), \\ \tilde{g}'(\theta) = y + 2f(\tilde{g}^2 + 2g_0\tilde{g}) + \left(\frac{3}{2} - 2r \right) (g_0 + \tilde{g})f^2 + r(r-1)f^3, \\ y'(\theta) = f^2 \left((q_0 + \tilde{q}) + 4g_0^2 f + 2g_0(g_0 + \tilde{g}) - \frac{3}{2}y \right), \\ \tilde{q}'(\theta) = -f^2 \left(\frac{1}{2}(q_0 + \tilde{q}) + b(xf + g_0 + \tilde{g}) \right). \end{cases} \quad (\text{B2})$$

Its linearization leads to

$$\frac{d}{d\theta} \tilde{Y} = L \tilde{Y} \quad \text{with} \quad \tilde{Y} = [\tilde{f}, \tilde{g}, \tilde{y}, \tilde{q}]^T \quad \text{and} \quad L := \begin{bmatrix} 0 & 0 & 0 & 0 \\ 0 & 0 & 1 & 0 \\ 0 & 0 & 0 & 0 \\ 0 & 0 & 0 & 0 \end{bmatrix}, \quad (\text{B3})$$

implying that all the eigenvalues of the linearized system are zero. Therefore, in order to study the dynamics near the stationary manifold S , we have to take into account the nonlinear corrections. Only one fixed point on S is relevant to our study, namely the origin $(f, g, p, q) = (0, 0, 0, 0)$. There are two orbits that enter/leave this point: they correspond to asymptotic behavior of our system at the front $\eta \rightarrow 1$ and at the tail $\eta \rightarrow \infty$. The nonlinear solutions for $\eta \rightarrow 1$ and for $\eta \rightarrow \infty$ are considered in Appendices D 1 and D 2 respectively. In terms of θ , these solutions read

$$(f, g, p, q) \rightarrow \left[C^{-1/2} (-2\theta)^{-3/4}, \frac{3}{2} C^{1/2} (-2\theta)^{-1/4}, -\frac{75}{8} C^{3/2} (-2\theta)^{-3/4}, -\frac{75}{8} C^{3/2} (-2\theta)^{-3/4} \right] \\ \text{as } \theta \rightarrow -\infty \quad (\eta \rightarrow 1). \quad (\text{B4})$$

and

$$(f, g, p, q) \rightarrow [b^{1/2}\theta^{-1/2}, -xb^{1/2}\theta^{-1/2}, A(3x-2)b^{3/2}\theta^{-3/2}, A(3-3x)b^{3/2}\theta^{-3/2}] \\ \text{as } \theta \rightarrow +\infty \quad (\eta \rightarrow \infty) \quad (\text{B5})$$

where $A = (r+x)(r+x-1)$.

When $|r| > 1/2$, there exist two other isolated fixed points,

$$P_{\pm} = \left(1, -\frac{1}{2}, -\frac{1}{3}, -1 \right) f_{\pm} \quad \text{with} \quad f_{\pm} := \pm \left(\frac{3}{2} \left(r^2 - \frac{1}{4} \right) \right)^{-1/2}, \quad (\text{B6})$$

with only point P_+ associated to positive spectrum being physical. The point P_+ is important for our scenario, because it is the change of stability properties of this point that marks the Hopf

bifurcation of the limit cycle creation. It is interesting that the position of P_+ is independent of the parameter x .

The isolated points (B6) exist in the 3D GW case ($d = 3, \alpha = 1$) for which $r = 2 > 1/2$ but not in the 3D NLS case ($d = 3, \alpha = 2$) for which $r = 1/2$. This means that the fourth-order model for the 3D NLS is degenerate; one could say that point P_+ then formally lies at infinity.

Linearizing the system (B1) around the stationary point P_+ , we obtain the following system

$$\tilde{X}'(\theta) = A\tilde{X}, \quad (\text{B7})$$

where $\tilde{X} = [\tilde{f}, \tilde{g}, \tilde{p}, \tilde{q}]^T$ denotes the vector of small perturbations. The matrix A has the following form

$$A = f_+^2 \begin{bmatrix} \frac{1}{2} & 1 & 0 & 0 \\ 3r^2 - r - 1 & -2r - \frac{1}{2} & -f_+^{-2} & f_+^{-2} \\ \frac{x}{1-2x} & \frac{1}{1-2x} & -\frac{3}{2} & 0 \\ \frac{x}{1-2x} & \frac{1}{1-2x} & 0 & -\frac{1}{2} \end{bmatrix}, \quad (\text{B8})$$

Hence, its characteristic polynomial $h(\zeta)$ reads

$$h(\zeta) = \det(A - \zeta E) = h_0\zeta^4 + h_1\zeta^3 + h_2\zeta^2 + h_3\zeta + h_4, \quad (\text{B9})$$

where

$$h_0 = 1, \quad h_1 = 2(r+1)f_+^2, \quad h_2 = -2f_+^2 + \left(4r + \frac{3}{4}\right)f_+^4, \quad (\text{B10})$$

$$h_3 = (b-4)f_+^4 + \frac{3}{2}f_+^6, \quad h_4 = -f_+^6. \quad (\text{B11})$$

We apply the Routh—Hurwitz stability criterion³⁶: *All roots of the polynomial $h(\zeta)$ have negative real parts if and only if*

$$\Delta_1 = h_1 > 0, \quad \Delta_2 = \begin{vmatrix} h_1 & h_3 \\ 1 & h_2 \end{vmatrix} > 0, \quad \Delta_3 = \begin{vmatrix} h_1 & h_3 & 0 \\ 1 & h_2 & h_4 \\ 0 & h_1 & h_3 \end{vmatrix} > 0, \quad \Delta_4 = h_4\Delta_3 > 0. \quad (\text{B12})$$

First, we consider the case Δ_3 and $\Delta_4 \neq 0$. Since $h_4 < 0$, then either Δ_3 or Δ_4 is less than zero. Therefore, the above criterion is not satisfied and all roots of the characteristic polynomial cannot be with negative real parts. Note that changing the direction of the time-like variable θ does not change the sign of $h_4 = \det(A) = \det(-A)$ and, therefore, does not change the fact of instability. Therefore, we conclude that the neighborhood of P_+ must always include stable and unstable orbits simultaneously.

Now consider the case $\Delta_3 = 0$ (hence $\Delta_4 = 0$ too). This is, in fact, the case of the Hopf bifurcation $x = x_H$ because it gives the condition which guarantees existence of two purely imaginary roots $\zeta_1 = i\omega$ and $\zeta_2 = -i\omega$ of the characteristic polynomial $h(\zeta)$. Indeed, it follows from Orlando's formula³⁶ for the polynomial $h(\zeta)$ that $\Delta_3 = 0$ if and only if the sum at least one pair of roots of $h(\zeta)$ is zero. Also since the determinant $h_4 = \det(A)$ of the matrix A is nonzero, and recalling that this determinant is equal to the product of all the eigenvalues, we have $\omega \neq 0$. But then, because $h_4 = \det(A) < 0$, and remembering that the roots of the real polynomial $h(\zeta)$ are either real or come in purely imaginary mutually conjugated pairs, the other two roots ζ_3 and ζ_4 are real numbers of different signs, $\zeta_3\zeta_4 < 0$.

To find x_H , we explicitly compute Δ_3 as

$$f_+^{-6}\Delta_3 = -f_+^{-4}b^2 - 2f_+^{-2}r(3r^2 - 7r - 4)b + 36r^5 - 51r^4 - 42r^3 + \frac{87}{4}r^2 + \frac{27}{2}r + \frac{3}{4} = 0, \quad (\text{B13})$$

where we recall $b = \frac{1}{2x-1}$. For example, for the case of the 3D GW system ($r = 2$) we get $x_H \approx 0.60014$, as identified by the numerical continuation software.

In addition to a pair of purely imaginary eigenvalues, the matrix $A(x_H)$ has an eigenvalue, ζ_3 or ζ_4 , with a positive real part. The resulting periodic orbit is unstable, as the eigenvalue with positive real part produces a Floquet exponent which in turn has a positive real part (see Remark 3 on p.20 in book³⁷). Changing the direction of time results in the changing the signs of both ζ_3 and ζ_4 . This does not alter the fact that one of these eigenvalues is positive. Thus, the emerging limit cycle is unstable in the case of the reversed time too. This fact makes it practically impossible to find the limit cycle numerically by directly computing the trajectories in the 4D phase space, because only measure-zero set of initial points would lead to orbits attracted to the cycle. This is another difference with the 2D case¹¹. Therefore, in order to find the cycles, we employ numerical continuation software, and specifically the PyCont library within the PyDSTool Python environment³¹ which is specially designed for finding unstable limit cycles; see Appendix C 2 .

Appendix C: Numerics

1. Numerical simulations and regularization

To simulate the transients of the fourth-order DAM, we use a log-discretization of the frequency spaces, and the grid points $\omega_i = 2^{i/\kappa}$, $i \in [-1200, 1200]$ where the parameter $\kappa = 20$ controls the

frequency binning. To regularize the system, we do not employ any viscosity but rather rely on smooth noise-robust differentiators³⁸ that compute derivatives in frequency space as

$$D[f, i] = \frac{42\delta_1 + 48\delta_2 + 23\delta_3 + 8\delta_4 + \delta_5}{512h\omega_i} \quad \text{with} \quad \delta_k := f_{i+k} - f_{i-k} \quad \text{and} \quad h = \kappa^{-1} \log 2. \quad (\text{C1})$$

We use the ADAM-Bashforth scheme of second-order to advance in time. Time steps are determined through the CFL condition:

$$\Delta t = \mu \times \min_{\omega} \frac{N + \epsilon}{|D_t N + \epsilon|} \quad \text{with} \quad \epsilon = 10^{-40} \quad \text{and} \quad \mu = 2^{-8} \text{ (GW) or } 2^{-11} \text{ (NLS)} \quad (\text{C2})$$

In all the cases reported here, the initial condition for the waveaction density $N(\omega)$ is a Gaussian centered at $\omega = 10^{13}$, with amplitude 10^{-5} and variance 0.1. Integration is made with the Python programming language³⁹ and sped-up using the *f2py* package⁴⁰.

2. Numerical continuation and the Simpson strategy

To “chase” the ∞_* -cycle, determine the anomalous exponent and generate the series of Figures 3, 4, 5, 6, we relied on the numerical continuation library PyCont package from the PyDSTool environment³¹, as described in Appendix A. Rather than computing its non-singular counterpart, it proved more efficient to deal with the original singular system (20).

Computing the branches of periodic solutions is straightforward in the generic case $\alpha \leq 1$, which includes the 3D GW case. In that case, the ∞_* -cycle is grown directly from the Hopf point at fixed α . After a series of bifurcations identified by the software as either *PD* or *LPC* points, the system converges towards x_* , and the convergence is increased upon decreasing the step-sizes and the numerical tolerance of the software. In our interpretation, the PD points flagged by the software appear to be spurious and the LPC points are genuine and represent the fold bifurcations discussed in the main text in relation to Fig. 3.

Computing the branches of periodic solutions is less straightforward when $\alpha > 1$ which, in particular, includes the 3D NLS case. Note that this range includes the non-generic cases $\alpha \geq 2$ but also the generic cases $1 < \alpha < 2$ for which the Hopf point is well-defined. Numerical continuations starting from the Hopf point then either fail to converge towards the ∞_* -cycle or simply cannot be initiated due to the Hopf points lying at ∞ . To generate the rather intricate patterns of

Fig. 4, the *Simpson strategy*⁴¹, however, proves very fruitful. The *Simpson strategy* consists of the three following steps illustrated in Panel (b) of Fig. 7 (i) Grow the cycles at fixed $\alpha = 1$ until the ∞_* -cycle is converged (up to some thresholds prescribed by the tolerance parameters), (ii) Bridge the 3D GW ∞_* -cycle to the desired $\alpha > 1$ by performing continuation with both α and x as free parameters, (iii) at desired α , freeze α and either grow or shrink the resulting cycle to check convergence towards ∞_* -cycle and generate associated branch of non-infinite periodic solutions. The outcome of the Simpson strategy is represented by the red lines in Panel (a) of Fig.7 which determine the behavior of x_* in the final phase portrait of Fig. 5.

To generate the full patterns of periodic branches at fixed $\alpha > 1$ as shown *e.g.* in Fig. 4 and in Panel (a) of Fig. 7, the same strategy is performed by modifying the step (i) of the Simpson strategy to stop the growth of the 3D GW cycle to some determined finite sizes rather than to the ∞_* cycle. All the numerics were done using a standard Dell XPS 13 laptop computer.

Appendix D: Asymptotics near the origin, $(f, g, p, q) \rightarrow 0$

Two relevant asymptotics near the fixed point $(f, g, p, q) \rightarrow 0$ correspond to the sharp front at $\eta \rightarrow 1$ and the power-law asymptotics and the power-law asymptotic at large η . Below, it will be easier for us to work with the original profiles $F, G = F', P, Q$ and the similarity variable η .

1. Solution near the sharp front, $\eta \rightarrow 1$.

Equation (14) can be represented as a system of four first-order differential equations for the variables $F, G = F', P$ and Q :

$$F' = G, \quad Q' = -b(xF + \eta G), \quad P' = -\eta b(xF + \eta G), \quad (\text{D1})$$

$$\eta^5 F^2 G' = r(r-1)\eta^3 F^3 + 2\eta^4 FG(\eta G - rF) + \eta Q - P. \quad (\text{D2})$$

We seek a solution near the frontal point, $\eta \rightarrow 1$ in the following asymptotic form

$$F(\eta) = C(\eta - 1)^\mu \quad (\text{D3})$$

with the positive constants C and μ to be found. Substituting this representation into the first equation in (D1), we have

$$G(\eta) = C\mu(\eta - 1)^{\mu-1}. \quad (\text{D4})$$

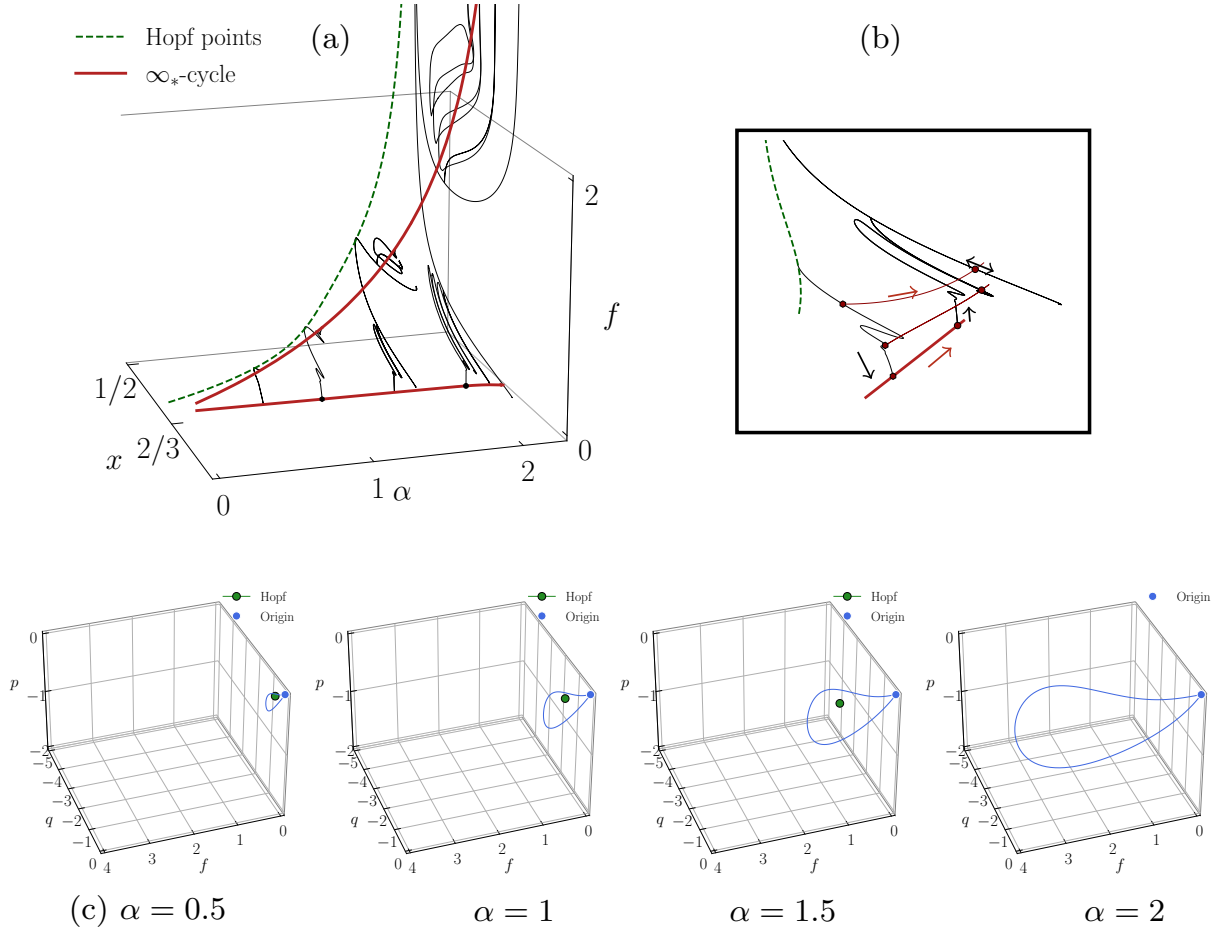


FIG. 7. **Numerical continuation of the ∞_* -cycle.** Panel (a) shows the extrema of f along the ∞_* -cycle (in red), obtained from the continuation of the GW ∞_* -cycle by continuous alteration of α and x_* . The black lines are continuation at fixed value of α , as in Fig. 3 and Fig. 4. Panel (b) illustrates the Simpson strategy described in §C 2 to find the branches of periodic solutions for $\alpha > 1$. Panel (c) shows the ∞_* -cycles for various values of α .

Substituting (D3) and (D4) into the two equations for P and Q , and integrating them, we get

$$P = C_P - C b(\eta - 1)^\mu - \frac{2\mu + x}{\mu + 1} C b(\eta - 1)^{\mu+1} - \frac{\mu + x}{\mu + 2} C b(\eta - 1)^{\mu+2}, \quad (\text{D5})$$

$$Q = C_Q - C b(\eta - 1)^\mu - C b \frac{\mu + x}{\mu + 1} (\eta - 1)^{\mu+1}, \quad (\text{D6})$$

where C_P and C_Q are constants. We are looking for a solution with zero fluxes P and Q at $\eta = 1$, so we put $C_P = C_Q = 0$. Substituting the expressions for F , G , P and Q in (D2), we get in the

leading order in $(\eta - 1)$:

$$\frac{C b}{\mu + 1}(\eta - 1)^{\mu+1} = C^3 \mu(\mu + 1)(\eta - 1)^{3\mu-2}. \quad (\text{D7})$$

To satisfy this equation, we must choose

$$\mu = \frac{3}{2}, \quad C = \sqrt{\frac{8b}{75}}. \quad (\text{D8})$$

2. Power-law asymptotics for $\eta \rightarrow \infty$.

Consider the solution for large η in a power law form,

$$F = C\eta^{-\nu}, \quad C > 0, \quad \nu > 0. \quad (\text{D9})$$

We proceed in the same way as for the frontal point. We substitute $F(\eta)$ into the first equation in (D1) and find the function $G(\eta)$. Then we substitute the functions $F(\eta)$ and $G(\eta)$ into the second and third equations in (D1) and, integrating them, find Q and P . Substituting the calculated functions in (D2), we get

$$C^3(\nu + r)(\nu + r - 1)\eta^{3-3\nu} + Cb\frac{\nu - x}{(\nu - 1)(\nu - 2)}\eta^{2-\nu} + C_Q\eta - C_P = 0, \quad (\text{D10})$$

where C_Q and C_P are the constants.

The first term has the leading order for $\nu \in (0, 1/2)$. But the prefactor for this term can be zero only for $\nu = -r$ or $\nu = 1 - r$. The second term is the leading one for $\nu \in (1/2, 1)$. To nullify this term, we must have $\nu = x$. The third term is of the leading order for $\nu > 1$. To cancel this term we must set $C_Q = 0$.

The two boundary values $\nu = 1/2$ and $\nu = 1$ require separate consideration. We have $C = 4/\sqrt{24r^2 - 6}$ for $\nu = 1/2$. For $\nu = 1$, the leading term vanishes only for $x = 1$. Thus, our choice of the large η asymptotics of $F(\eta)$ as a power law with the exponent $\nu = x$ is consistent with the values of x in the interval $(1/2, 1)$.